ANALYTICAL MODEL FOR ELECTRIC MACHINE SIZING IN ELECTRIFIED AVIATION

Victor Bahrs*, Martin Staggat* and Lars Enghardt *

* German Aerospace Center (DLR), Institute of Electrified Aero Engines, Department: Architecture of Propulsion System, Lieberoser Str. 13a, 03046 Cottbus, Germany

Abstract

Decreasing green-house gas emissions and thus reducing the impact on climate warming is one of the biggest challenges in modern aviation industry. Significantly emission reduction for an aircraft will only be possible with novelty propulsion systems. Fully or partially electrified topologies represent one category of novel aircraft propulsion systems. These new powertrain architectures need to be designed from scratch and require a detailed theoretical investigation. To analyse the potential of different powertrain topologies a modelling of the electrified components has to be done. A central component of electrified propulsion is an electric machine, which transforms electrical into mechanical power. The present study introduces an analytical model for the sizing of a permanent magnet synchronous electric machine. The analytical character of the model allows fast and little computationally intensive calculations and is therefore optimal for fundamental considerations about new electrified aircraft powertrain topologies. The major benefit of the presented model is the linking of the sizing process to the efficiency calculation of the electric machine. Among the most important geometric parameters of the motor the model also accounts for the thermal limitations of the machine. Thus, it is possible to size the volume, mass and efficiency of the machine simultaneously.

Keywords

Electric Machine Sizing; Analytical Model; PMSM; Air Cooled; Electrified Aircraft

NOMENCLATURE

Symbols

α_p	Ratio Pole-arc / Pole-pitch	$[-]$
α_R	Ratio Resistance AC / DC	$[-]$
δ	Skin Depth	[m]
η	Efficiency	$[\%/100]$
κ	Conductivity	$[\mathrm{S/m}]$
λ	Relative Length	$[-]$
μ	Permeability	$[-]$
ω	Angular Speed	$[1/\mathrm{s}]$
ρ	Density	$[\mathrm{kg/m^3}]$
σ	Stress	[Pa]
φ	Phase Shift	[deg]
A	Electric Loading	$[\mathrm{A/m}]$
B	Magnetic Loading	$[\mathrm{Wb/m^2}]$
b	Width	[m]
d	Diameter	[m]
f	Frequency	[Hz]
h	Height	[m]
I	Current	[A]
J	Current Density	$[\mathrm{A/m^2}]$
k	Fill Factor	$[-]$
l	Length	[m]
m	Mass	[kg]
N	Number	$[-]$
n	Rotational Speed	[Hz]
P	Power	[W]
Q	Torque	[Nm]
R	Resistance	[Ω]
r	Radius	[m]
S	Surface Area	$[\mathrm{m^2}]$
U	Voltage	[V]
V	Volume	$[\mathrm{m^3}]$
v	Surface Speed	$[\mathrm{m/s}]$

doi: 10.25967/570099

Indices

Cu	Copper
Fe	Iron
mag	Magnet
mot	Motor
p	Stator Pole
ph	Phase
rms	Root Mean Square
rot	Rotor
sha	Shaft
sl	Sleeve
t	Stator Turn
w	Wire

Acronyms

AC	alternating current
DC	direct current
PMSM	permanent magnet synchronous machine

1. INTRODUCTION

In order to address man-made climate change, ambitious political goals have been formulated. The Advisory Committee of aviation research and innovation in Europe (ACARE) has summarized its targets up to the year 2050 in the "Flightpath 2050" resolution. This strategy paper specifies that in 2050, compared to the reference year 2000, an aircraft should achieve a reduction of nitrogen oxides by 90% and carbon dioxide emissions by 75%. [1] In order to achieve these goals innovations must be made, particularly in the area of aircraft propulsion systems. One possible approach for reducing green-house gas emissions in aviation is the electrification of aircraft engines. By using electrical energy from renewable sources to produce emission free fuels like hydrogen or to store it in batteries, an emission free aircraft propulsion can be realized. For the electrification of aircraft powertrains by a fuel cell using hydrogen or a battery, electric motors are one fundamental component. Electric machines are used to transform electric into mechanical energy and finally into thrust. To reach the long time goal of emission free aircraft propulsion the electric motors have to be light and as compact as possible accompanied by a high efficiency. It is assumed that electric motors in a time frame to 2035 will need power densities between $9 - 16\,\mathrm{kW/kg}$ with efficiencies up to $99\,\%$ to met the specific requirements for electric flight [2–4]. To reach these power densities the motor has to be considered with the total powertrain and existing interdependences. Thus models which have a high detail degree and are little computationally intensive are required for initial design studies. Therefore the hereafter described electric machine model follows an analytical approach. The central benefit of the introduced model is the interlinking of the sizing process with the efficiency calculation. Notwithstanding the analytical approach the model allows furthermore a high geometric detail degree and taking basic thermal limitations into account.
Recent studies indicate that permanent magnet synchronous machines (PMSM) seem to be the most promising motor topology to reach high power densities for aviation application [5–7]. Therefore the introduced model sizes a PMSM regarding the volume, mass and efficiency.

2. METHODS

The introduced electric motor model is based on an analytical approach. It sizes a permanent magnet synchronous machine by assuming the geometric structure visualised in figure 1 and 2 regarding mass, volume and efficiency.

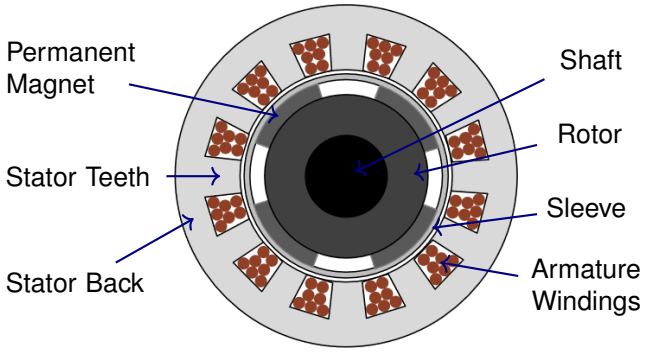

FIG 1. Cross section of modelled permanent magnet synchronous motor

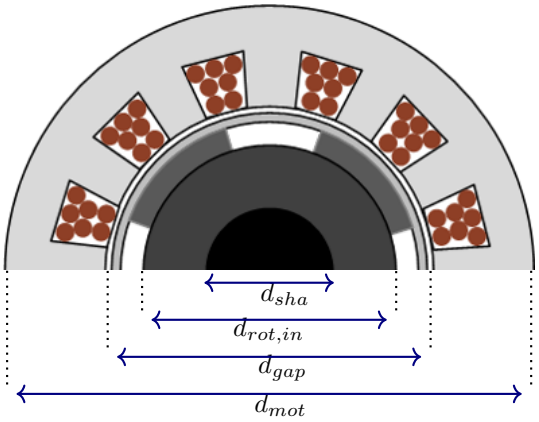

FIG 2. Cross section and diameter definition

2.1. Sizing

The mechanical power P_{mech} of an electric motor can be calculated with the apparent motor power P_S, the efficiency η and the power factor $cos(\varphi)$ [8].

$$P_{mech} = P_S \cdot \eta \cdot cos(\varphi) \tag{1}$$

The apparent power of an electric machine can be described as the product of the machines rotational speed n and the torque Q [9].

$$P_S = 2\pi \cdot n \cdot Q \tag{2}$$

The torque of an electric machine is directly dependent on the machine size and the electric and magnetic load [9]. Using this dependency and the angular rotational speed $\omega = 2\pi n$, equation (2) can be rewritten as:

$$P_S = \frac{\pi}{2} \cdot \overline{B} \cdot \overline{A} \cdot d_{gap}^2 l \cdot \omega \tag{3}$$

The effective electric and magnetic load are $\overline{A}$ and $\overline{B}$ respectively. Equation (3) shows that the electric machine power is proportional to the squared active motor diameter d_{gap} and the motor length l. The diameter and length are values of the active machine, meaning the part of the machine that transforms the electric to mechanic power. By this dependence it is possible to size the machine active volume based on the needed motor power.

Based on this approach different machine sizing formulas were established and can be found in the literature [10–13]. Reshaping equation (3) leads to:

$$d_{gap}^2 l = \frac{P_S}{\frac{\pi}{2} \cdot \overline{B} \cdot \overline{A} \cdot \omega} \tag{4}$$

In different publications various correction factors were used to cover i.e. machine geometry influences. Another way to include dependencies on machine parts such as magnets can be performed by calculating the electric and magnetic load based on the corresponding field densities. The electric load can be calculated through equation (5) [14, 15], the magnetic load is approximated in first order according to [5] by equation (6).

$$\overline{A} = \frac{N_t \cdot N_{ph} \cdot I_{rms}}{\pi \cdot r} \tag{5}$$

N_{ph} and N_t represent the number of phases and turns per phase respectively, while I_{rms} is the effective current and r is the radius of the motor.

Assuming a sinusoidal course, the effective magnetic load can be calculated through equation (7).

$$\widehat{B} = \frac{B_r}{1 + \frac{h_{gap}}{h_{mag}}} \tag{6}$$

$$\overline{B} = \frac{\widehat{B}}{\sqrt{2}} \tag{7}$$

The magnetic load is influenced by the remanent magnetic field density B_r of the used permanent magnets, the magnet height h_{mag} and the gap thickness between magnet and armature windings h_{gap}. The gap thickness is calculated by the addition of the air gap h_{air} and the sleeve thickness h_{sl}. This approximation is reasonable because both, the used sleeve material carbon fibre and air are non magnetic [16].

$$h_{gap} = h_{air} + h_{sl} \tag{8}$$

The required air gap can be approximated according to [17] dependent on the motor power and pole number (9), while equation (10) is used to calculate the sleeve thickness [18].

$$h_{air} = \frac{C_1 + C_2 \cdot P^{0.4}}{1000} \tag{9}$$

Pole number	C_1	C_2
$N_p = 2$	0.2	0.01
$N_p > 2$	0.18	0.006

TAB 1. Factors air gap calculation [17]

$$h_{sl} = -\frac{m_{mag} r_{sl} \omega_{max}^2}{\pi l (\rho_{sl} r_{sl}^2 \omega_{sl}^2 - \frac{\sigma_{y,sl}}{K_{sl}})} \tag{10}$$

As defined in equation (10) the sleeve thickness is dependent on the magnet mass m_{mag}, the sleeve radius, motor length, angular velocity and sleeve material properties like the yield stress $\sigma_{y,sl}$ or density ρ_{sl}. To secure safe sleeve operation, the material yield stress is divided by a security factor K_{sl}.

Applying the equations (1) and (5) - (7) to equation (4), a formula for the product of machines active diameter and length can be found:

$$d_{gap} l = \frac{\sqrt{2} \cdot P_{mech}}{I_{rms} \cdot N_t \cdot N_{ph} \cdot \widehat{B} \cdot \omega \cdot \eta \cdot cos(\varphi)} \tag{11}$$

$$\lambda = \frac{l}{d_{gap}} \cdot \frac{N_p}{\pi} \tag{12}$$

The relative length λ of a motor from equation (12) is used to calculate the active diameter from equation (11) [8]. Thus the rotor diameter can be calculated.

$$d_{rot} = d_{gap} - 2 \cdot h_{air} \tag{13}$$

With the resulting rotor diameter d_{rot} the surface speed v is determined:

$$v = d_{rot} \cdot \pi \cdot \omega \tag{14}$$

If the maximum allowed surface speed is exceeded a different relative length has to be chosen (cf. fig 5). The maximum allowed surface speed is according to [6] set to $v_{max} = 250\,\mathrm{m/s}$.
When this boundary condition holds true, the sleeve thickness is iterated with the magnet mass by equation (15).

$$m_{mag} = \alpha_p \cdot \frac{\pi}{4} \cdot \left[(d_{rot,in} + 2 \cdot h_{mag})^2 - d_{rot,in}^2\right] \cdot l \cdot \rho_{mag} \tag{15}$$

The total magnet mass is thereby determined by the ratio of pole pitch to pole arc α_p at the inner rotor diameter from equation (16). With an optimal ratio between $0.7 \leq \alpha_p \leq 0.75$ [19] the mass and therefore required sleeve thickness (eq. (10)) can be calculated.

$$d_{rot,in} = d_{gap} - 2 \cdot (h_{air} + h_{sl} + h_{mag}) \tag{16}$$

Because the magnet mass is dependent on the sleeve thickness h_{sl} and vice versa, the determination of the sleeve thickness needs an iteration (cf. fig 5). Following the sleeve mass can be calculated by equation (17).

$$m_{sl} = \frac{\pi}{4} \cdot \left[d_{rot}^2 - (d_{rot} - 2 \cdot h_{sl})^2\right] \cdot l \cdot \rho_{sl} \tag{17}$$

With the new sleeve thickness h_{sl} the magnetic loading $\widehat{B}$ has to be recomputed. The recalculated loading is used as new input to the sizing process and iterated until the loading is not changing anymore (cf. fig 5).
With the torque Q, the yield torsion stress of the shaft material σ_t and a security factor K_{sha} the minimal required shaft diameter d_{sha} is calculated by equation (18) [20]. Thereafter the inner rotor diameter $d_{rot,in}$ is checked against the minimal required shaft diameter and in doubt the relative length is recomputed again (cf. fig 5). Since two conditions have to be met for the relative length during the sizing it is possible, that a motor is not valid sizeable by the given set of input parameters.

$$d_{sha} = \sqrt[3]{\frac{16 \cdot Q \cdot K_{sha}}{\pi \sigma_t}} \tag{18}$$

Having the rotor sized, the stator can be addressed. In a first step the teeth and slot widths need to be determined. Using the combined width of one teeth and slot $b_{teeth,slot}$ from equation (19) and the dependency of the teeth to slot width ratio on the slot height in figure 3, the width of one teeth and slot can be identified. The therefore required slot height h_{slot} can be calculated by equation (20) [6] with an initial guess of the slot width b_{slot}. An iteration of this procedure results in the final width (cf. figure 5).

$$b_{teeth,slot} = \frac{\pi \cdot d_{gap}}{N_{slots}} \tag{19}$$

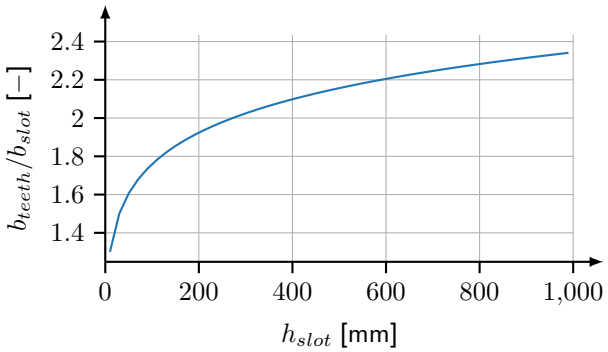

FIG 3. Ratio of the teeth and slot width as a function of the slot height (data extract from [21, S. 521])

$$h_{slot} = 2 \cdot b_{slot} \tag{20}$$

With the resulting slot height the coil diameter d_{coil} (21), the area of the slots S_{slot} (22) and teeths S_{teeth} (23) and the yoke height h_{yoke} (24) (acc. to [21]) are defined:

$$d_{coil} = d_{gap} + 2 \cdot h_{slot} \tag{21}$$

$$S_{slot} = \frac{b_{slot,in} + b_{slot,out}}{2} \cdot h_{slot} \tag{22}$$

$$S_{teeth} = \frac{b_{teeth,in} + b_{teeth,out}}{2} \cdot h_{slot} \tag{23}$$

$$h_{yoke} = 1.5 \cdot b_{slot} \tag{24}$$

Taking thermal limitations from an air cooled electric machine into account, Grauers et. al. [21] determined a dependence between the slot height and allowed current density in the windings showed in figure 4.
With the relation from figure 4 the allowed current density J is identified and the diameter of the copper wires in the stator windings d_w (25) and the resulting wire area S_w (26) can be calculated with respect to the effective motor phase current I_{rms}.

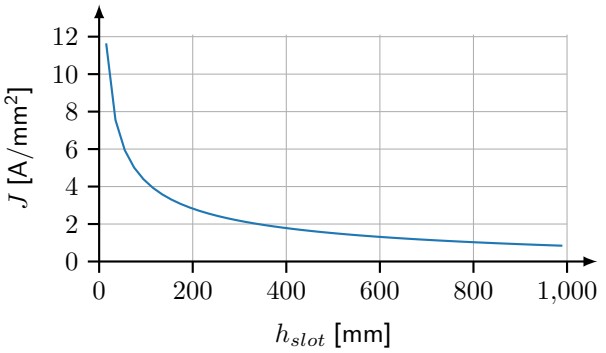

FIG 4. Allowed current density taking thermal limitations into account (data extract from [21, S. 522])

$$d_w = \sqrt{\frac{I_{rms} \cdot 4}{J \cdot \pi}} \tag{25}$$

$$S_w = \frac{\pi}{4} \cdot d_w^2 \tag{26}$$

Using a copper fill factor k and the total number of slots and phases, the number of coil turns per phase is calculated by equation (29).

$$S_{slot,Cu} = S_{slot} \cdot k \tag{27}$$

$$S_{ph,Cu} = \frac{S_{slot,Cu} \cdot N_{slots}}{N_{ph}} \tag{28}$$

$$N_t = \frac{S_{ph,Cu}}{S_w} \tag{29}$$

As visualized in figure 5 the number of stator turns N_t is returned to the start of the sizing process and iterated until the number isn't changing anymore.

Subsequent the wire length is calculated (30) by the motor length and the end winding length, which is determined by the motor coil diameter and the number of poles assuming distributed winding.

$$l_w = 2 \cdot l + 2 \cdot \frac{d_{coil}}{N_p} \tag{30}$$

Finally the total motor diameter d_{mot} (31) and volume V_{mot} (32) are determined. The equations (33) - (38) are used to calculate the motor parts and total masses.

$$d_{mot} = d_{gap} + 2 \cdot (h_{slot} + h_{yoke}) \tag{31}$$

$$V_{mot} = \frac{\pi}{4} \cdot d_{mot}^2 \cdot l \tag{32}$$

$$m_{sha} = \frac{\pi}{4} \cdot d_{sha}^2 \cdot l \cdot \rho_{sha} \tag{33}$$

$$m_{rot} = \frac{\pi}{4} \cdot \left[d_{rotor}^2 - d_{sha}^2 \right] \cdot l \cdot \rho_{rot} \tag{34}$$

$$m_{coil} = \frac{\pi}{4} \cdot d_w^2 \cdot l_w \cdot N_{ph} \cdot N_t \cdot \rho_{coil} \tag{35}$$

$$m_{teeth} = S_{teeth} \cdot N_{slots} \cdot l \cdot \rho_{teeth} \tag{36}$$

$$m_{yoke} = \frac{\pi}{4} \cdot \left[d_{mot}^2 - d_{coil}^2 \right] \cdot l \cdot \rho_{yoke} \tag{37}$$

$$m_{mot} = m_{sha} + m_{rot} + m_{mag} + m_{sl} + m_{teeth} + m_{coil} + m_{yoke} \tag{38}$$

2.2. Efficiency calculation

The losses appearing in a PMSM are dominated by three sources: the electrical losses in the armature windings, magnetic losses in the stator iron and mechanical losses resulting from the machine rotation. [8, 17]

The electrical losses per phase $P_{j,ph}$ are dependent on the effective current I_{rms} and the phase resistance R_{ph} [8]:

$$P_{j,ph} = R_{ph} \cdot I_{rms}^2 = R_{ph} \cdot \left(\frac{\widehat{I}}{\sqrt{2}} \right)^2 \tag{39}$$

The DC resistance of the coil $R_{DC,coil}$ in one phase is calculated with equation (40) [8].

$$R_{DC,coil} = \frac{N_t \cdot l_w}{S_w \cdot \kappa} \tag{40}$$

Considering that the resistance of a wire increases, when AC is used instead of DC, equations (41) and (42) are applied [22, 23].

$$R_{ph} = R_{AC} = \alpha_R \cdot R_{DC,coil} \tag{41}$$

(42)

$$\alpha_R = \begin{cases} 1 & f < 1/x_R \\ 1 + [d_w/(4\delta)]^4/3 & 1/x_R \leq f \leq 4/x_R \\ 0.25(d_w/\delta)^2/(d_w/\delta - 1) & f > 4/x_R \end{cases}$$

with: $x_R = \pi \mu \kappa r_w^2$

The AC frequency is denoted by f while δ represents the skin depth, which can be calculated by equation (43) [22]. The wire conductivity and permeability are symbolized by κ and μ respectively.

$$\delta = \frac{1}{\sqrt{\pi f \mu \kappa}} \tag{43}$$

With the electrical losses per phase and the assumption of a three-phase motor, the total electrical losses can be determined as follows:

$$P_j = 3 \cdot P_{j,ph} \tag{44}$$

The magnetic losses P_{vu} resulting from the remagnetization of the stator are dependent on the magnetic field density in the iron $\hat{B}_1$, the iron mass m_{Fe}, specific power losses $\nu_{u1.5}$ and a frequency dependent correction factor $F(f)$ [8].

$$P_{vu} = k_u \nu_{u1.5} \left(\frac{\hat{B}_1}{1.5\,\mathrm{T}} \right)^2 \cdot m_{Fe} \cdot F(f) \tag{45}$$

The frequency dependent correction factor $F(f)$ consists of specific hysteresis $\sigma_{hyst1,5}$ and eddy currents losses $\sigma_{wb1,5}$.

$$F(f) = \frac{\sigma_{hyst1,5}}{\nu_{u1.5}} \cdot \left(\frac{f}{50\,\mathrm{Hz}} \right) + \frac{\sigma_{wb1,5}}{\nu_{u1.5}} k_{wb1} \cdot \left(\frac{f}{50\,\mathrm{Hz}} \right)^2 \tag{46}$$

With the dependencies from equation (47) the frequency correction factor can be determined without exact knowledge of the typical losses parts [8]. The typical specific iron losses and the corrections coefficients k are listed in table 2.

$$\begin{aligned} \nu_{u1.5} &= \sigma_{hyst1,5} + \sigma_{wb1,5} \\ \sigma_{hyst1,5} &= (0.5...0.9) \cdot \sigma_{wb1,5} \end{aligned} \tag{47}$$

Parameter	Symbol	Unit	Value
specific iron losses	$\nu_{u1.5}$	[W/kg]	2.5
correction coefficient teeth	$k_{u,teeth}$	[–]	$1.7 - 2.5$
correction coefficient yoke	$k_{u,yoke}$	[–]	$1.5 - 1.8$
correction coefficient higher harmonics	k_{wb1}	[–]	1
roughness coefficient	k_{rou}	[–]	1

TAB 2. Specific loss calculation parameters [8, 17]

Equation (48) is used to calculate the mechanical losses [17]. Mechanical losses are mostly dominated by the windage losses from the cylindrical assumed rotor. Therefore equation (48) is divided in the losses from the rotating cylinder mantle $P_{\rho w1}$ and the losses occurring at the flat end plates of the cylinder $P_{\rho w2}$.

$$P_{\rho w} = P_{\rho w1} + P_{\rho w2} \tag{48}$$

The losses of the cylinder mantle area are determined with equation (49). They are dependent on the rotor diameter and length, the rotational speed, as well as on the torque C_{M1} and roughness coefficient k_{rou} (cf. table 2) and the density of the surrounding fluid ρ_{air}. [17]

$$P_{\rho w1} = \frac{1}{32} k_{rou} C_{M1} \pi \rho_{air} \omega^3 d_{rot}^4 l_{rot} \tag{49}$$

The torque coefficient C_{M1} is available by equation (50) with dependence on the reynolds couette number Re_δ (51) [17].

$$C_{M1} = \begin{cases} 10 \cdot \frac{(2h_{air}/d_{rot})^{0.3}}{Re_\delta} & Re_\delta < 64 \\ 2 \cdot \frac{(2h_{air}/d_{rot})^{0.3}}{Re_\delta^{0.6}} & 64 < Re_\delta < 5 \cdot 10^2 \\ 1.03 \cdot \frac{(2h_{air}/d_{rot})^{0.3}}{Re_\delta^{0.5}} & 5 \cdot 10^2 < Re_\delta < 10^4 \\ 0.065 \cdot \frac{(2h_{air}/d_{rot})^{0.3}}{Re_\delta^{0.2}} & 10^4 < Re_\delta \end{cases} \tag{50}$$

$$Re_\delta = \frac{\rho_{air} \omega d_{rot} h_{air}}{2\mu} \tag{51}$$

The windage losses at the end plates (52) are again dependent on the rotational speed, the surrounding fluid density as well as on the the rotor and shaft diameter. The torque coefficient C_{M2} is identified by the tip reynolds number Re_r (54) and equation (53) [17].

$$P_{\rho w2} = \frac{1}{64} C_{M2} \rho_{air} \omega^3 (d_{rot}^5 - d_{sha}^5) \tag{52}$$

$$C_{M2} = \begin{cases} \frac{3.87}{Re_r^{0.5}} & Re_r < 3 \cdot 10^5 \\ \frac{0.146}{Re_r^{0.2}} & Re_r > 3 \cdot 10^5 \end{cases} \tag{53}$$

$$Re_r = \frac{\rho_{air} \omega d_{rot}^2}{4\mu} \tag{54}$$

To take additional electromagnetic losses into account P_{add} is calculated for permanent magnet synchronous machines with (55) [17].

$$P_{add} = \frac{0.15}{100} \cdot P \tag{55}$$

With the addition of all determined losses the total loss power (56) and the motor efficiency (57) can be calculated. As visualized in figure 5 the efficiency is a sizing input and has to be iterated.

$$P_{loss} = P_j + P_{vu} + P_{\rho w} + P_{add} \tag{56}$$

$$\eta = \frac{P}{P + P_{loss}} \tag{57}$$

3. RESULTS AND DISCUSSION

3.1. Validation of the motor model

The validation of the described analytical electric motor model is done with available data from commercial motors. A bunch of air cooled PMSM from the companies MGM Compro, MagicAll and Geiger Engineering, which are listed in the appendix table 4, are used for the validation.
The rated power and rotational speed of the comparison motors are used as input parameters of the model. Furthermore the machines diameter to length ratio is kept the same compared to the real motors. A detailed list of input parameters can be found in the appendix table 5.

In figure 6 the validation of the modelled machine volume is shown. The volume calculated by equation (32) is in a very good agreement to the comparison motor volumes. The total coefficient of determination is $r^2 = 0.988$. Despite some difference of up to 30% for individual motors, the regression curves nearly collapses. Based on this validation the sizing model is able to deliver accurate volume data for PMSMs.

The validation of the mass calculated by the model shows significantly greater differences to the comparison motor masses (cf. figure 7). This may be caused by small differences in the motor geometry between the model and the compared motors. It may further indicate that the motors are built by materials with lower densities then the assumed ones. With the material densities from table 5 the modelled motor masses are up to twice as high then the data published by the manufacturers.

The efficiency validation in figure 8 determines a nearly constant offset of $3 - 5\,\%$. This can be attributed to manufacture dependent losses that are almost impossible to represent in a model. Manufacturing processes like cutting or packaging the stator iron sheets for example impact the resulting motor losses [24]. The trend of higher efficiencies with higher power ratings can be found in the modelled data as well as in the validation motor data.

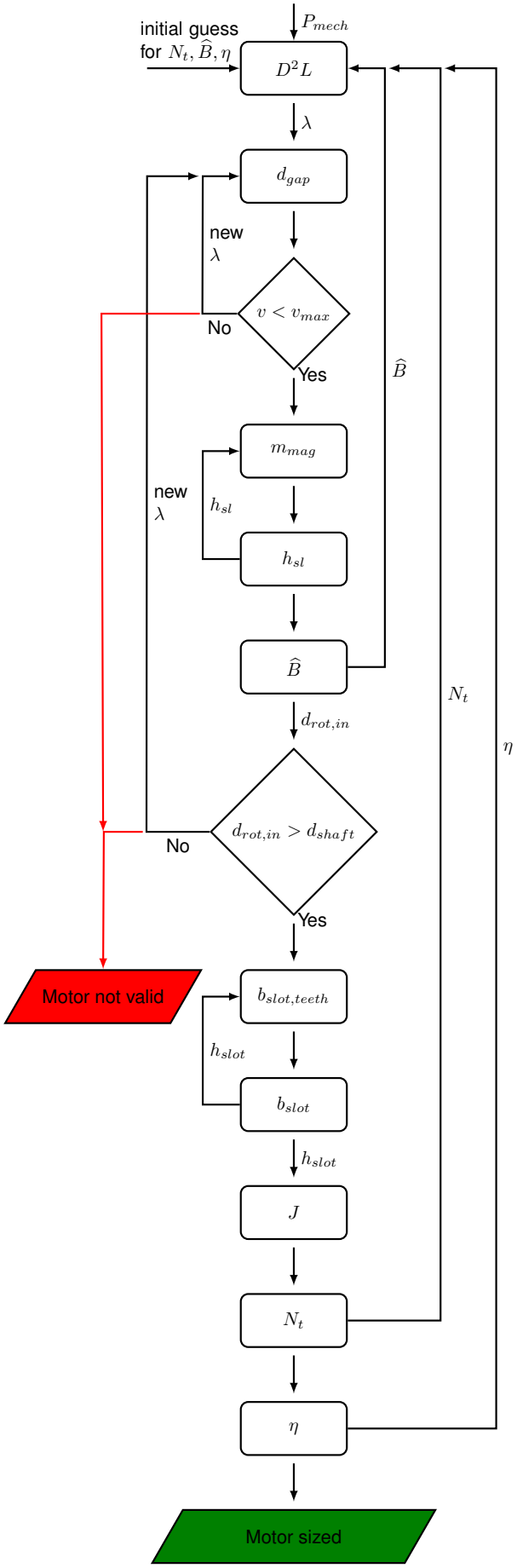

FIG 5. Sizing logic

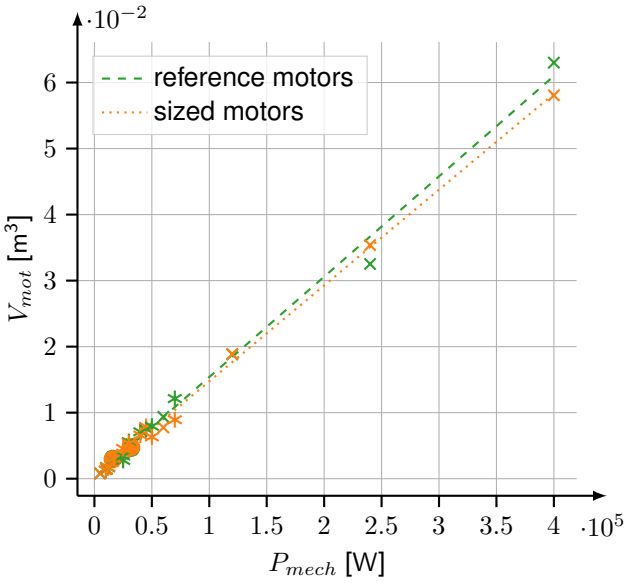

FIG 6. Volume Validation

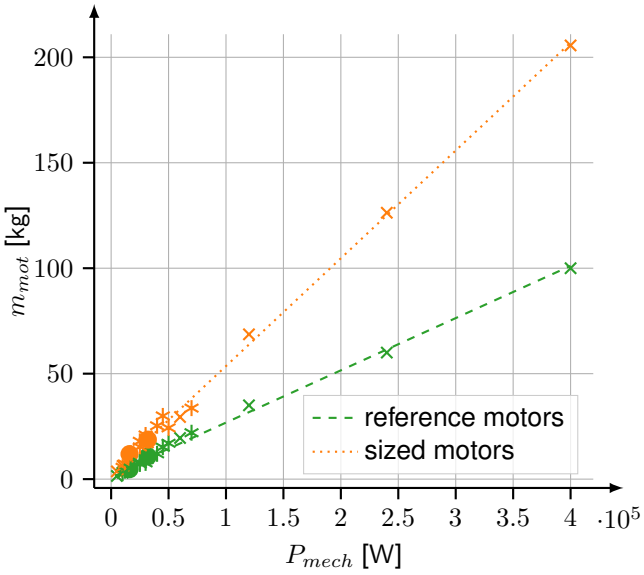

FIG 7. Mass Validation

Summarized the validation of the model shows, especially for the volume, a good agreement with the motor data used for comparison.

3.2. Parameter study

After the successful model validation the parameters listed in table 3 are varied and analysed regarding the mass, volume and efficiency of a 100 kW electric motor. Furthermore listed is the variation range and impact that the parameters have on the motor.
The default values used for motor sizing can be find in the appendix table 5.

Figure 9 shows a significant dependency of the rotational speed on the motor mass. Especially at low rotational speeds the required motor mass increases drastically. This behaviour results from

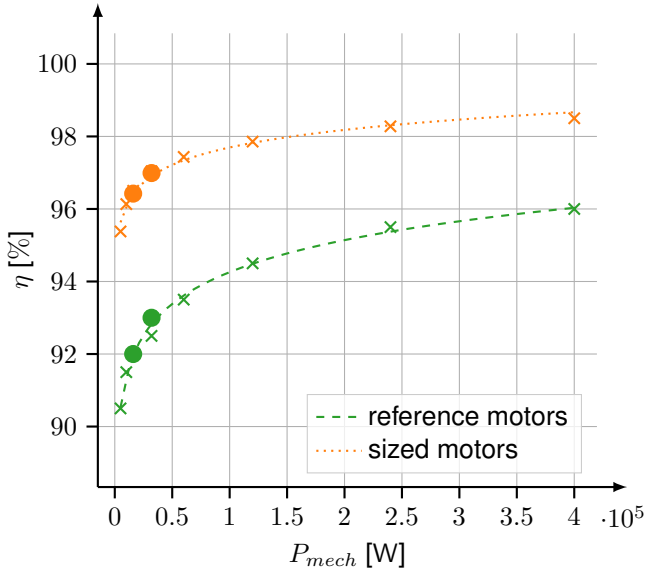

FIG 8. Efficiency Validation

Parameter	Unit	Value Range	Impact
rotational speed	[Hz]	$5 - 60$	high
copper fill factor	[–]	$0.1 - 0.9$	high
number of poles	[–]	$4 - 16$	medium
magnet height	[mm]	$1 - 25$	medium
relative length	[–]	$0.5 - 2$	low

TAB 3. Variation of parameters

the dependence of motor power, rotational speed and torque (cf. equation (2)). At low rotational speed the torque has to increase, which results in an increased motor volume and thus mass. Due to the larger motor the electric, magnetic and mechanic losses also increases, which leads to a decreased efficiency at low rotational speeds. While the motor mass gets smaller with increasing rotational speed, the efficiency reaches a maximum value between 45 Hz. This results from the higher mechanical and frequency dependent magnetic losses at higher rotational speeds which cause the efficiency to decrease above 45 Hz.

The copper fill factor in the stator slots has as well a significant impact to the motor sizing (cf. figure 10). With a higher fill factor more stator windings fit into one slot. Thus the electric torque is increasing which leads to a decreasing size and mass of the motor. Especially for fill factors below 0.2 the motor mass increases significantly. The efficiency curve shows a similar behaviour to the rotational speed variation. At small fill factors the efficiency is low due to the higher losses caused by the bigger motor. At approximately $k = 0.4$ the efficiency starts to decrease again. This is caused by the rising copper losses while increasing the fill factor. A higher copper fill factor will also lead to a larger heat output caused by the electric losses.

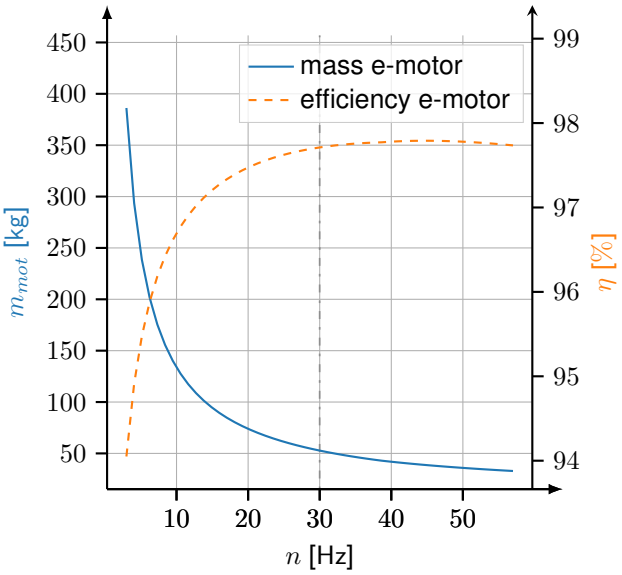

FIG 9. Variation of the motor rotational speed at 100 kW

Thus the current density maybe has to be decreased at high fill factors, which is not considered in the model.

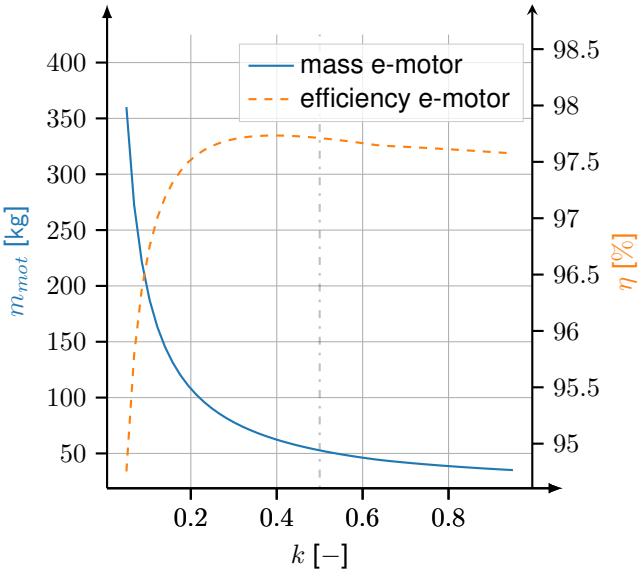

FIG 10. Variation of the copper fill factor at 100 kW

Figure 11 shows, that the pole number has as smaller impact on the motor mass and efficiency than the rotational speed or the fill factor. With an increasing number of poles, the mass and efficiency both decrease. An increase of the pole number implies an increase of the number of slots whereby the width of one slot gets smaller. With the dependence from figure 4 the current density can be raised which leads to a higher torque. Also the yoke height reduces due to the dependency from equation (24). As a result the motor mass decreases. Furthermore the electric losses get higher due to the raised current density which results in a decreased efficiency.

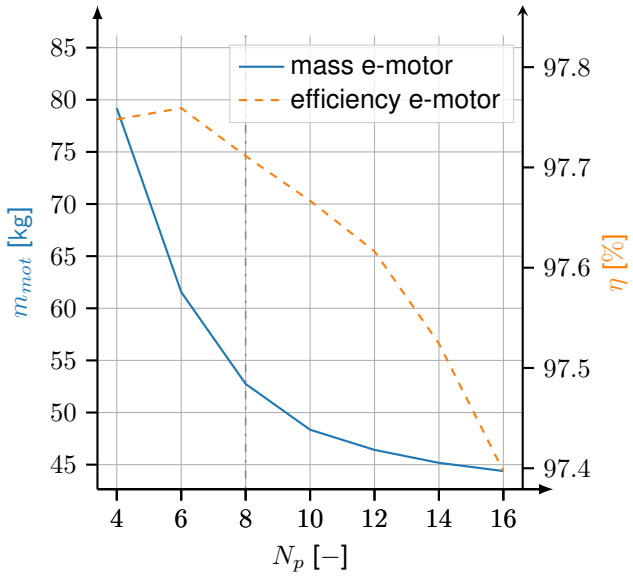

FIG 11. Variation of the number of poles at 100 kW

The trend of the motor volume in figure 12 is differing from the mass for the variation of the number of poles. The motor volume has a minimum value at a pole number of $N_p = 8$. A further raising of the number of poles decreases the torque due to the smaller slots and thus fewer number of windings. Thereby the air gap diameter has to increase which results in a higher volume of the motor. While the volume is rising at $N_p > 8$, the mass still reduces because the yoke height continues to become smaller, which results in a decreased iron mass.

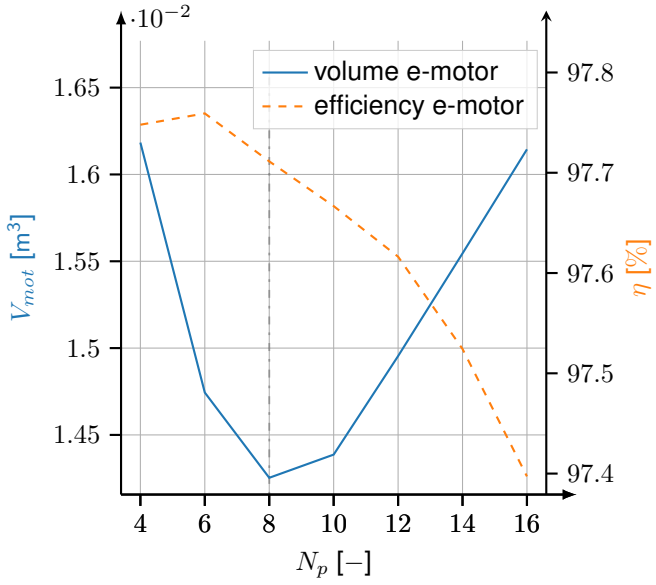

FIG 12. Variation of the number of poles at 100 kW

Figure 13 shows the variation of the magnet height. Regarding the mass of the motor an optimal height can be determined. The efficiency is rising with increasing magnet height. Greater magnets results in an increased magnetic load and thereby a smaller motor size and mass. The higher magnet

weight though require as well a raised sleeve thickness, which leads to a decreased magnetic load and a higher motor size and mass (eq. (6), (10)). These contrary dependences results in a minimal motor mass for a magnet height of approximately $h_{mag} = 7\,\text{mm}$.

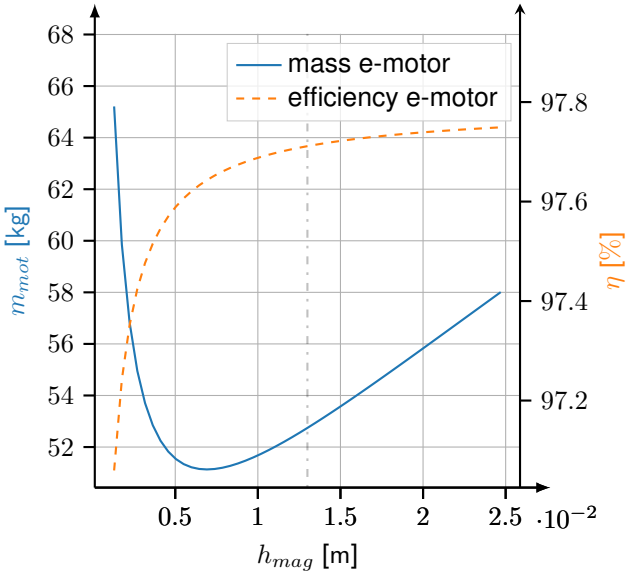

FIG 13. Variation of the magnet height at 100 kW

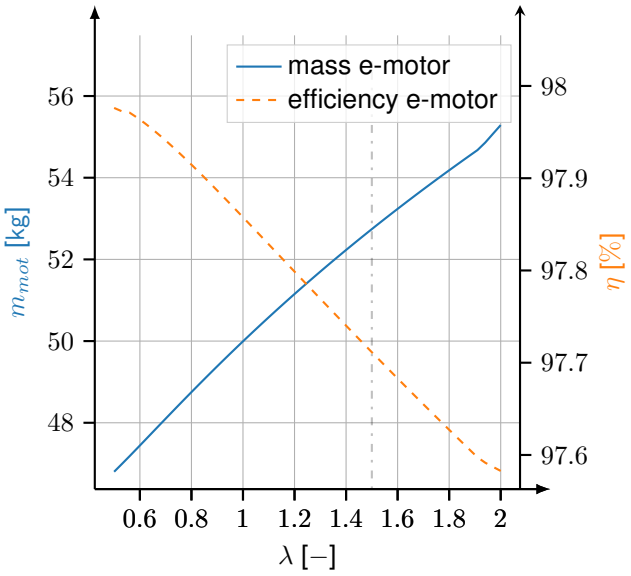

FIG 14. Variation of the motor relative length at 100 kW

Figure 14 shows the variation of the relative length and thereby the motor diameter to length ratio. An increased relative length results in a mass growth and an efficiency loss. Meaning that a greater diameter compared to the length has a positive outcome for motor size, mass and efficiency. However, the impact of the relative length is rather small. The smaller the diameter becomes compared to the length, the fewer space the stator teeths and slots have. The resulting reduction of stator turns and increase of current density leads to a small efficiency reduction and motor mass rise. Realistically limits for the minimal length or maximum diameter of a motor exist, whereby it is not possible to decrease the relative length without limitations.

3.3. Efficiency map

With the presented model of electric machines it is furthermore possible to calculate motor defining efficiency maps. Therefore a design point is used to size the electric motor with its given input parameter, which is marked in the maps by a black point. Based on the sized motor the rotational speed and the power is varied and the efficiency is calculated in this off-design points. With a grid of different rotational speed and power or rather torque values, it is possible to draw an efficiency map.
To include the voltage dependence on the rotational speed in off-design calculation, the voltage factor K_v is used. The terminal voltage in off-design points is calculated by equation (58) [25].

$$U_{off-design} = \frac{\omega}{K_v} + I_{rms} \cdot R_{sta} \tag{58}$$

The voltage factor is approximated by equation (59) with the design point of the motor [26].

$$K_v = \frac{\omega_{design}}{U_{design} - I_{rms,design} \cdot R_{ph}} \tag{59}$$

The motor is designed at a power of 100 kW and the input parameters listed in table 5. Figure 15 shows the efficiency map in dependence of torque and rotational speed, while figure 16 visualize the efficiency in dependence of power and rotational speed.
Until the design rotational speed $n = 30\,\text{Hz}$ the power is increasing up to the design power of 100 kW, while the torque remains constant. A further increase of the rotational speed leads to flux weakening effects accompanied by a decreasing torque. Therefore the region of rotational speeds above the design speed is modelled as constant in power at decreasing torque.

The maximum efficiency of approximately $97\,\%$ is reached in the vicinity slightly below the design rotational speed. In this speed region the efficiency remains nearly maximal even when reducing the power or rather the torque.
Very low efficiencies are determined for coupling of low power and high torque or high rotational speed values. In this regions the torque or rather rotation dependent losses dominate, which leads to low efficiencies.

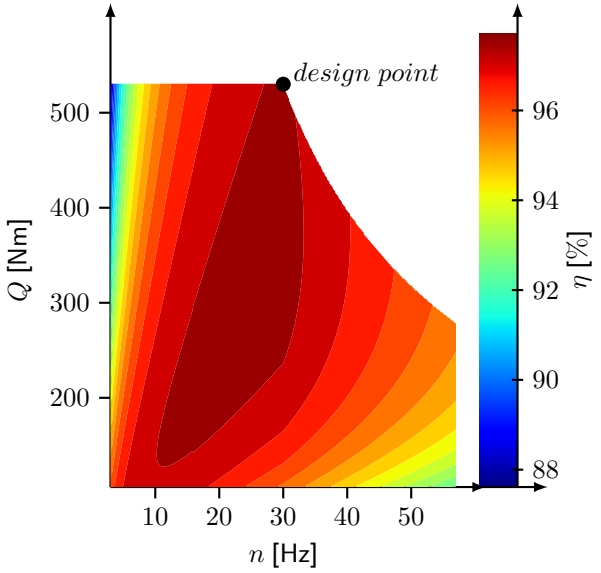

FIG 15. Efficiency map rotational speed & torque

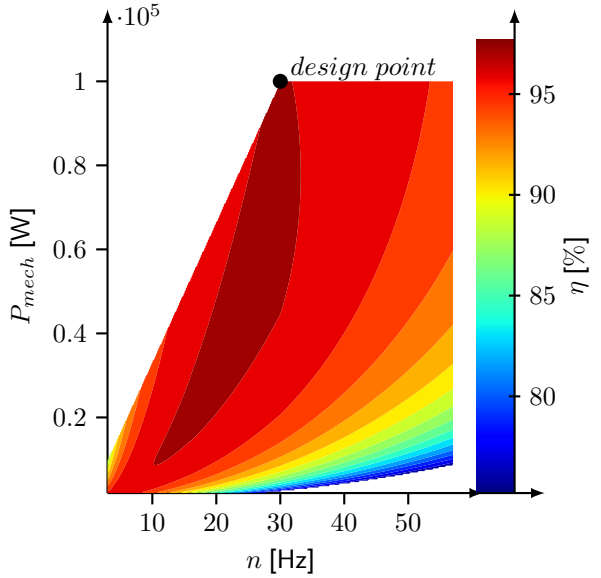

FIG 16. Efficiency map rotational speed & power

4. CONCLUSION

In this paper an analytical model for a permanent magnet synchronous machine sizing is presented. The model involves a large set of motor parameters describing the geometry and performance. Furthermore it couples the efficiency calculation and the sizing process. The model was validated against commercial motors, which showed a good agreement regarding the volume, mass and efficiency. The validated motor model allows a detailed sizing and thus can be used to analyse the impact of motor parameters and the dependencies between them. Furthermore the model enables the possibility to study the interdependencies between the motor and the motor controller or rather a complete powertrain with low computational costs.
Therefore the model can be used in studies of electrified aero engines which offer a pathway towards emission free aircraft propulsion.

Contact address:

victor.bahrs@dlr.de

References

[1] Europäische Kommission, Generaldirektion Mobilität und Verkehr, and Generaldirektion Forschung und Innovation. *Flightpath 2050 : Europe's vision for aviation : maintaining global leadership and serving society's needs*. Publications Office, 2011. DOI: doi/10.2777/50266.

[2] Ehab Sayed, Mohamed Abdalmagid, Giorgio Pietrini, Nicole-Marie Sa'adeh, Alan Dorneles Callegaro, Cyrille Goldstein, and Ali Emadi. Review of electric machines in more-/hybrid-/turbo-electric aircraft. *IEEE Transactions on Transportation Electrification*, 7(4):2976–3005, 2021. DOI: 10.1109/TTE.2021.3089605.

[3] D.K. Hall, E.M. Greitzer, A.P. Dowdle, J.J. Gonzalez, B. Yutko, C. Courtin, W. Thalheimer, L. Trollinger, J. Tylko, N. Varney, A. Uranga, S. Byahut, and M. Kruger. Feasibility of electrified propulsion for ultra-efficient commercial aircraft: Final report: Nasa. 2019.

[4] Xiaolong Zhang, Cheryl L. Bowman, Tim C. O'Connell, and Kiruba S. Haran. Large electric machines for aircraft electric propulsion. *IET Electric Power Applications*, 12(6):767–779, 2018. DOI: 10.1049/iet-epa.2017.0639.

[5] Mykhaylo Filipenko, Stefan Biser, Martin Boll, Matthias Corduan, Mathias Noe, and Peter Rostek. Comparative analysis and optimization of technical and weight parameters of turbo-electric propulsion systems. *Aerospace*, 7(8):107, 2020. DOI: 10.3390/aerospace7080107.

[6] Dipl. Eng. M.D. Bogomolov. Concept study of 20 mw highspeed permanent magnet synchronous motor for marine propulsion.

[7] Wenping Cao, B. C. Mecrow, G. J. Atkinson, J. W. Bennett, and D. J. Atkinson. Overview of electric motor technologies used for more electric aircraft (mea). *IEEE Transactions on Industrial Electronics*, 59(9):3523–3531, 2012. DOI: 10.1109/TIE.2011.2165453.

[8] Germar Müller, Karl Vogt, and Bernd Ponick. *Berechnung elektrischer Maschinen*, volume 2. Band of *Elektrische Maschinen / Germar Müller*. Wiley-VCH Verlag GmbH & Co. KGaA, Weinheim, 6., völlig neu bearbeitete auflage edition, 2008. ISBN: 3527405259.

[9] Austin Hughes. *Electric motors and drives: Fundamentals, types, and applications*. Elsevier/Newnes, Amsterdam, fourth edition edition, 2013. ISBN: 9780080983325.

[10] Surong Huang, Jian Luo, F. Leonardi, and T. A. Lipo. A general approach to sizing and power density equations for comparison of electrical machines. *IEEE Transactions on Industry Applications*, 34(1):92–97, 1998. DOI: 10.1109/28.658727.

[11] Shihua Wu, Weiwei Fan, and Shumei Cui. Sizing equations suitable for driving motor initial design. In *2014 IEEE Conference and Expo Transportation Electrification Asia-Pacific (ITEC Asia-Pacific)*, pages 1–3. IEEE, 31.08.2014 - 03.09.2014. DOI: 10.1109/ITEC-AP.2014.6941045.

[12] Aaron D. Anderson, Nathaniel J. Renner, Yuyao Wang, Dongsu Lee, Shivang Agrawal, Samith Sirimanna, Kiruba Haran, Arijit Banerjee, Matthew J. Starr, and James L. Felder. System weight comparison of electric machine topologies for electric aircraft propulsion. In *2018 AIAA/IEEE Electric Aircraft Technologies Symposium*, Cincinnati, Ohio, 2018. American Institute of Aeronautics and Astronautics. DOI: 10.2514/6.2018-4983.

[13] Samith Sirimanna, Balachandran Thanatheepan, Dongsu Lee, Shivang Agrawal, Yangxue Yu, Yuyao Wang, Aaron Anderson, Arijit Banerjee, and Kiruba Haran. Comparison of electrified aircraft propulsion drive systems with different electric motor topologies. *Journal of Propulsion and Power*, 37(5):733–747, 2021. DOI: 10.2514/1.B38195.

[14] Jacek F. Gieras, Rong-Jie Wang, and Maarten J. Kamper. *Axial flux permanent magnet brushless machines*. Springer, New York, 2nd ed. edition, 2008. ISBN: 9781402069932.

[15] C. D. Sanabria von Walter. *Design of high-torque-density synchronous drives for propulsion of rotary-wing aircraft*. Delft University of Technology, 2016. ISBN: 978-94-6186-648-6.

[16] M. Koledintseva, P. C. Ravva, R. DuBroff, J. Drewniak, K. Rosanov, and B. Archambeault. Engineering of composite media for shields at microwave frequencies. In *2005 International Symposium on Electromagnetic Compatibility, 2005. EMC 2005*, pages 169–174. IEEE, 2005. DOI: 10.1109/ISEMC.2005.1513494.

[17] Juha Pyrhonen, Tapani Jokinen, and Valeria Hrabovcová. *Design of rotating electrical machines*. Wiley, Chichester West Sussex United Kingdom and Hoboken NJ, 2008. ISBN: 9780470695166.

[18] Francesco Cupertino, Riccardo Leuzzi, Vito Monopoli, and Giuseppe Cascella. Design procedure for high-speed pm motors aided by optimization algorithms. *Machines*, 6(1):5, 2018. DOI: 10.3390/machines6010005.

[19] Z. J. Liu and J. T. Li. Accurate prediction of magnetic field and magnetic forces in permanent magnet motors using an analytical solution. *IEEE Transactions on Energy Conversion*, 23(3):717–726, 2008. DOI: 10.1109/TEC.2008.926034.

[20] Alfred Böge. *Formeln und Tabellen zur technischen Mechanik*. Studium. Vieweg + Teubner, Wiesbaden, 22., erw. aufl. edition, 2011. ISBN: 9783834814456.

[21] A. Grauers and P. Kasinathan. Force density limits in low-speed pm machines due to temperature and reactance. *IEEE Transactions on Energy Conversion*, 19(3):518–525, 2004. DOI: 10.1109/TEC.2004.832059.

[22] Yaojia Zhang, Li Wang, and Lexuan Meng. An analytical ac resistance calculation method for multiple-conductor feeder cables in aircraft electric power systems. *IEEE Transactions on Industrial Electronics*, 67(5):3340–3349, 2020. DOI: 10.1109/TIE.2019.2917417.

[23] Alan Payne. Skin effect, proximity effect and the resistance of circular and rectangular conductors, 2016.

[24] David Bauer. *Verlustanalyse Bei Elektrischen Maschinen Für Elektro- und Hybridfahrzeuge Zur Weiterverarbeitung in Thermischen Netzwerkmodellen*. Wissenschaftliche Reihe Fahrzeugtechnik Universität Stuttgart Ser. Springer Fachmedien Wiesbaden GmbH, Wiesbaden, 2019. ISBN: 9783658242725.

[25] Mark Drela. First-order dc electric motor model: Mit aero & astro. 2007.

[26] Patrick Vratny. Investigation of universally electric propulsion systems for transport aircraft.

[27] Magicall motors. https://www.magicall.biz/products/integrated-motor-controller-magidrive/. Accessed: 2022-09-01.

[28] Mgm compro motors. https://www.mgm-compro.com/electric-motors/. Accessed: 2022-09-01.

[29] Geiger engineering motors. https://www.geigerengineering.de/avionik/produkte. Accessed: 2022-09-01.

[30] Tian-Hua Liu, Yi Chen, Pei-Heng Yi, and Jui-Ling Chen. Integrated battery charger with power factor correction for electric–propulsion systems. *IET Electric Power Applications*, 9(3):229–238, 2015. DOI: 10.1049/iet-epa.2014.0168.

[31] Phil H. Mellor, Rafal Wrobel, and Neville McNeill. Investigation of proximity losses in a high speed brushless permanent magnet motor.

[32] Ralph Funck. Composite materials in high efficient sleeve applications of electric machines.

[33] Herbert Wittel, Dieter Muhs, Dieter Jannasch, and Joachim Voßiek. *Roloff/Mattek Maschinenelemente: Normung, Berechnung, Gestaltung*. Vieweg + Teubner, Wiesbaden, 19., überarb. und erw. aufl. edition, 2009. ISBN: 9783834806895.

[34] M.A.K. Chowdhuri and R.A. Hossain. Design analysis of an automotive composite drive shaft. *International Journal of Engineering and Technology*, 2010.

[35] Waelzholz. Elektrobandwerkstoffe und lacksysteme.

A. APPENDIX

A.1. Motor validation motors

Company	Model	Power [kW]	Symbol
MAGicALL	6	5	x
MAGicALL	12	10	x
MAGicALL	20	16	x
MAGicALL	40	32	x
MAGicALL	75	60	x
MAGicALL	150	120	x
MAGicALL	300	240	x
MAGicALL	500	400	x
Geiger Engineering	HPD 16	16	●
Geiger Engineering	HPD 32D	32	●
MGM COMPRO	REB 30	30	⋆
MGM COMPRO	REB 50	40	⋆
MGM COMPRO	REB 60	45	⋆
MGM COMPRO	REB 90	70	⋆
MGM COMPRO	RET 20	10	⋆
MGM COMPRO	RET 30	12	⋆
MGM COMPRO	RET 60	25	⋆
MGM COMPRO	REX 30	17	⋆
MGM COMPRO	REX 50	25	⋆
MGM COMPRO	REX 90	50	⋆

TAB 4. List of commercial motors used for model validation [27–29]

Parameter	Symbol	Unit	Value	Source
rotational speed	n	[Hz]	30	-
number of phases	N_{ph}	[−]	3	-
number of poles	N_p	[−]	8	-
power factor	$\cos\varphi$	[−]	0.95	[30]
magnet flux density	B_r	[−]	1.17	[17]
height magnet	h_{mag}	[m]	$13 \cdot 10^{-3}$	-
relative length	λ	[−]	1.5	[8]
magnetic field density iron teeth	$\hat{B}_{1,teeth}$	[T]	1.8	[8]
magnetic field density iron yoke	$\hat{B}_{1,yoke}$	[T]	1.3	[8]
copper fill factor	k	[−]	0.5	[31]
yield stress sleeve	$\sigma_{y,sl}$	[Pa]	$1440 \cdot 10^6$	[32]
yield stress shaft torsion	$\sigma_{t,zul}$	[Pa]	$125 \cdot 10^6$	[33]
security factor sleeve	K_{sl}	[−]	3	[18]
security factor shaft	K_{sha}	[−]	3	[34]
density shaft	ρ_{sha}	[kg/m^3]	7800	[33]
density rotor	ρ_{rot}	[kg/m^3]	1000	- [a]
density magnet	ρ_{mag}	[kg/m^3]	7400	[17]
density sleeve	ρ_{sl}	[kg/m^3]	2100	[32]
density coil	ρ_{coil}	[kg/m^3]	8900	[33]
density teeth	ρ_{teeth}	[kg/m^3]	7600	[35]
density yoke	ρ_{yoke}	[kg/m^3]	7600	[35]

[a] Assuming a material saving construction with free spaces between struts, the density of the rotor is set to a lower value than steel or iron.

TAB 5. List of input parameters